Stimulated Raman Side Scattering in Laser Wakefield Acceleration

T. Matsuoka, C. McGuffey, P. G. Cummings, Y. Horovitz,* F. Dollar, V. Chvykov, G. Kalintchenko, P. Rousseau, V. Yanovsky, S. S. Bulanov, A. G. R. Thomas, A. Maksimchuk, and K. Krushelnick

Center for Ultrafast Optical Science and FOCUS Center, University of Michigan, Ann Arbor, Michigan 48109 USA

(Received 11 February 2010; published 14 July 2010)

Stimulated Raman side scattering of an ultrashort high power laser pulse is studied in experiments on laser wakefield acceleration. Experiments and simulations reveal that stimulated Raman side scattering occurs at the beginning of the interaction, that it contributes to the evolution of the pulse prior to wakefield formation, and also that it affects the quality of electron beams generated. The relativistic shift of the plasma frequency is measured.

DOI: 10.1103/PhysRevLett.105.034801 PACS numbers: 41.75.Jv, 52.27.Ny, 52.35.Mw

Stable propagation of ultrashort laser pulses having focused intensities exceeding the relativistic threshold ($\sim 10^{18}$ W/cm^2) in low density plasmas is an important requirement for laser wakefield accelerators (LWFAs) [1–3]. LWFAs have become a very promising potential application because of the high quality quasimonoenergetic electron beams that have been observed [4–6]. Subsequent experimental developments have extended the electron beam energy to the GeV range using plasma guiding structures [7], and also have reduced the energy spread to the order of a percent [8].

The self-guided LWFA regime [3,9] in which the laser pulse is guided over a long distance via relativistic self-focusing [2,3,10–14] is attractive because of its simplicity when compared to the use of plasma guiding structures. However, in such experiments the acceleration process is significantly affected by laser pulse evolution and propagation instabilities because of the high laser intensities required. For example, if the laser pulse breaks into filaments [12,14], a stable wakefield structure cannot occur, and therefore characteristics of the electron beam such as beam spatial profile, emittance, and energy spread are degraded when compared with the stable propagation of a single laser filament.

In this Letter, we report on the first systematic experimental study of stimulated Raman side scattering (SRSS) of an ultrashort pulse laser and its correlation to the high energy electron beams produced by LWFA at very high laser power. Stimulated Raman scattering is the coupling of an intense laser pulse (of frequency ω_0) to an electron plasma wave (ω_p) and a scattered light wave (such that $\omega_{sc} = \omega_0 - \omega_p$). This instability can contribute to evolution of the laser pulse prior to electron beam production in the "bubble" regime [2–6,15]. Numerical simulations reveal that the laser pulse is etched via the process of SRSS. We also demonstrate experimentally that SRSS is enhanced by larger focal spots—which is likely due to the longer transverse distance across the spot over which the instability can grow. In addition, these observations enable us to measure for the first time the wavelength shift of the scattered SRSS (i.e., the relativistically corrected plasma frequency)—which is useful as an *in situ* spatially resolved measure of the laser intensity during propagation.

In the experiments, an interaction pulse ($\lambda_0 = 800$ nm, $\tau = 35$ fs) irradiated a helium gas jet from a supersonic nozzle. The length of the gas jet was 2–3 mm in the experiments discussed here. Two focusing configurations were used, $f/10$ and $f/15$, in order to study the influence of laser focusing on SRSS in a LWFA. In the $f/10$ configuration, after wave front correction with a deformable mirror, the 10 cm diameter laser beam was focused using a 1 m focal-length off-axis parabolic mirror to a spot of 10 μm FWHM containing 60% of the pulse energy [16]. A focused peak intensity of 8×10^{19} W/cm^2 was achieved using a laser power of 100 TW. In the $f/15$ configuration, the laser beam was focused by a 1.5 m focal-length off-axis parabolic mirror without wave front correction. In this case, 32% of the laser energy was in an elliptical focal spot of FWHM major and minor axes of 31 and 16 μm, respectively, and hence a focused peak intensity of 1×10^{19} W/cm^2 was achieved using 100 TW laser power. For all of the experiments described here the contrast ratio between the amplified stimulated emission on the nanosecond time scale and the pulse peak was 10^{-8}. A probe pulse was generated by splitting 4% from the interaction pulse using a 2 μm thick pellicle for interferometry.

A shearing interferometer was used in the probe arm to measure the plasma density profile with spatial resolution ~ 10 μm. Accelerated electrons produced in the interaction were deflected by a sector shaped magnet and were measured by a LANEX (Kodak) scintillating screen. Light emitted by the LANEX screen was imaged by a lens onto another CCD camera through a BG-39 (Schott Glass) filter. The energy scale on the LANEX screen is nonlinear and the resolution was ± 5 MeV for 50 MeV electrons, and ± 7 MeV for 100 MeV, which was limited by the electron beam divergence of 10 mrad. The transmitted laser beam was reflected by a glass wedge and was sent to an imaging system in order to measure the laser mode image and spectrum.

Typical interferograms of the plasma are shown in Figs. 1(a) and 1(d) for different laser powers. Both inter-

ferograms show a plasma column generated from ionization of the gas by the laser pulse along the laser axis. These images were obtained during experiments using the $f/15$ configuration. The transverse size of the plasma column is 300–400 μm and is larger than the focal spot diameter due to the existence of lower intensity wings of the pulse. At the top of Fig. 1(d) above the plasma column there are relatively smaller fringe shifts and narrow filamented structures (bounded by dashed arrows k_{s1} and k_{s2}, which indicate the wave vector whose scattering angle ϕ shows maximum and minimum, respectively [Fig. 1(h)]. This structure is likely due to the significant scattered energy from the laser pulse via SRSS and the filamented ionization patterns are due to a ''bursting'' behavior of this instability in the nonlinear regime [17]. This SRSS is symptomatic of an unmatched interaction with a laser pulse longer than the relativistic plasma wavelength as shown later by simulations. For unmatched pulses, stimulated Raman scattering (SRS) is excited and the pulse also undergoes erosion or compression until it becomes about half of the plasma wavelength. When SRSS occurs at low levels as shown in Fig. 1(a), a single laser spot (b) similar to the vacuum focus (g) is typically observed at the exit of the plasma. This stable laser beam propagation generally generates a single, quasimonoenergetic electron bunch as shown in Fig. 1(c). However, when the laser power is increased, SRSS increases dramatically and the laser pulse is more likely to break up into filaments. Laser filamentation can contribute to the production of multiple beamlets of electrons with a broad energy spectrum due to the strongly time dependent nature of the interaction as shown in Fig. 1(f). In these experiments this structure is only observed in the upper half plane for all shots, which is likely due to the asymmetrical focal spot of the laser.

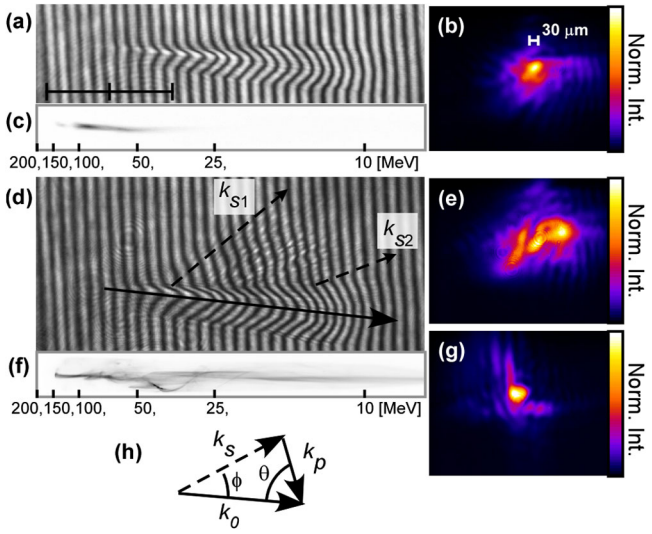

FIG. 1 (color online). (a) and (d) Interferogram, (c) and (f) electron spectrum, (b), (e), and (g) laser mode images. (h) Vector diagram of scattering. Sets of images (a)–(c) and (d)–(f) are obtained for a single shot of laser power at 26 TW and 95 TW, respectively. The plasma density is 2.5 and 2.9×10^{19} cm^{-3}. The spatial scale in (a) is 0.5 mm per division. In (d), the laser propagation axis (k_0: laser wave vector) is shown by the black solid arrow, and the ionized region due to side scattered light showing maximum and minimum scattering angles (ϕ measured from k_0) is indicated by k_{s1} and k_{s2}, respectively. The intensity scale of laser mode images is normalized to peak intensity for each image. (b) and (e) show mode images at the exit of the gas jet, while (g) shows the focal spot in vacuum. The intensity of image (c) is multiplied by 10.

The scattering angle for the maximum growth rate of SRSS depends on plasma density and is shown in Fig. 2 for k_{s2}. A formula derived from the wave number matching condition, where forward and backward SRS produce the same wave number density perturbation [18], can be expressed as

$$\sin\phi = \cos\theta = \sqrt{2\omega_{\rm pr}/\omega_0}, \quad (1)$$

where θ is the angle between plasma wave vector (k_p) and the laser pulse, the relativistic corrected plasma frequency is given by $\omega_{\rm pr} = \omega_p/\sqrt{\gamma}$ with $\gamma = \sqrt{1 + a_0^2/2}$, and a_0 is the normalized vector potential, $a_0 = 0.85 \times 10^{-9}\ \lambda_{\mu\rm m}\sqrt{I[\rm W/cm^2]}$. The focal spot diameter and the pulse duration in vacuum were used to estimate a_0 in Fig. 2. The angle of k_{s2} demonstrates good agreement with the above expression but not k_{s1}, which is 10–20 degrees greater than the angles for k_{s2}. The characteristic angle observed in the experiment changes to smaller values as the beam propagates through the plasma.

In experiments using the $f/10$ configuration we also imaged the side scattered spectrum perpendicular to both the laser polarization and laser propagation directions. In order to adjust the laser polarization, a half wave plate was inserted after pulse compression in vacuum. The electron generation and spot size were not affected by the wave plate. The spatially resolved spectrum is shown in Fig. 3 for different laser intensities. The laser intensity was decreased by changing the laser energy and pulse duration. The plasma density profile was measured from transverse interferometry as discussed earlier. The on-axis density

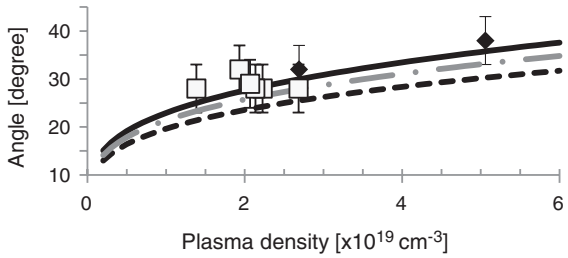

FIG. 2. Plasma density dependence of scattered light angle, ϕ, from (diamonds) 30 TW shots and (squares) 100 TW shots. The lines are from Eq. (1) at (solid) $a_0 = 0$, (dash-dotted), $a_0 = 1.2$, and (dashed) $a_0 = 2.1$. Nonzero a_0 values are consistent with vacuum focus diameter for laser power of 30 and 100 TW. The error bar corresponds to variation of k_0 including focusing cone angle, i.e., 3.8°.

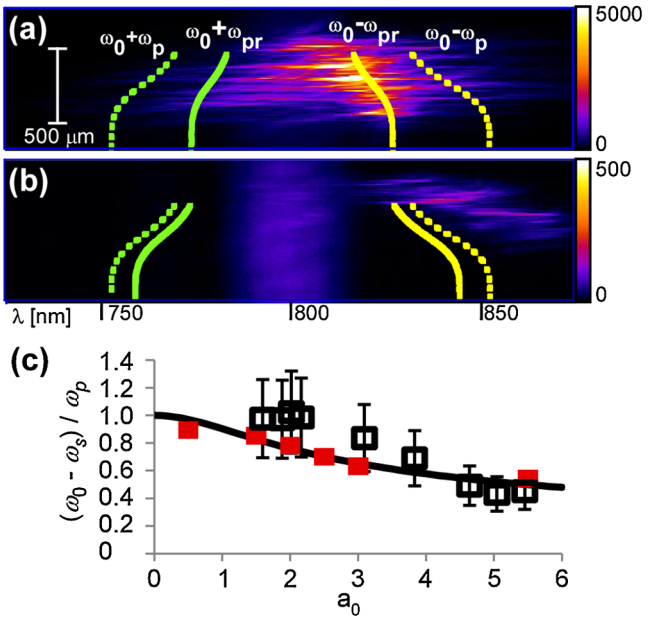

FIG. 3 (color online). Spatially resolved spectrum of side scattering light. (a) $a_0 = 4.8$, $\tau = 35$ fs, $E = 2.3$ J. (b) $a_0 = 1.3$, $\tau = 170$ fs, $E = 0.96$ J. Here E is laser energy. The vertical axis is the spatial axis. The laser pulse propagates from top to bottom. SRSS satellites' lines are overlaid on images as indicated. Emission around 800 nm in (b) is due to the probe pulse and is too weak to measure in (a). (c) Frequency shift as a function of laser intensity. Open (solid) squares are experimental (simulation) data points. The solid curve is ω_{pr}. Error bars are due to density gradients within the observation window. Each data point is an average of 1–6 shots.

profile was used to calculate ω_p, which was subsequently used to estimate the satellite wavelength through $\omega_{sc} = \omega_0 \pm \omega_p$. However, the linear SRSS expression was found to not correlate to the experimentally measured satellites, as in addition to a density dependence, there was also an observed intensity dependence.

The relativistically corrected plasma scattered frequency $\omega_{scr} = \omega_0 \pm \omega_{pr}$ consequently needs to be considered. Here, the focal spot diameter and the pulse duration in vacuum were used to estimate a_0. Scattered light was observed consistently from the first 500 μm of propagation, which is comparable to the Rayleigh range of the laser pulse. The spectral peak is shifted according to the relativistically corrected ω_{pr} along the propagation axis rather than the ω_p for high intensity interaction as shown by Fig. 3(a). No anti-Stokes component was observed in these experiments, which is consistent with linear SRS theory [19]. For lower intensity interactions where $a_0 \sim 1.3$ [Fig. 3(b)], the spectral shift is best represented by the linear plasma frequency, ω_p. The spatial dependence of the frequency shift in Fig. 3 is due to the density increase at the front of the gas jet. It should also be noted that in the forward direction, there is no clear observation of SRS (either as scattered Stokes or anti-Stokes lines). Intensity dependence is clearly observed as shown in Fig. 3(c), which shows the frequency shift ($\omega_s - \omega_0$) as a function of a_0 over a wide parameter range ($\tau = 35$–240 fs, $E = 0.96$–3.3 J, and $n_e = 0.74$–1.2×10^{19} cm^{-3}). Here, the frequency shift is obtained from a point where the maximum SRSS signal is observed in individual images. Note that data points from experiments and simulations agree well with ω_{pr}, although the focal spot diameter and the pulse duration in the vacuum are used to estimate a_0. The measured frequency shift is therefore useful as a spatially resolved diagnostic of laser intensity in plasmas. The product of the growth and time given by the SRS backscattering growth rate can be written as $G_{SRS} = a_0 \tau \sqrt{\omega_0 \omega_{pr}/2}$ [19] and can be used to estimate gain of the instability in the linear regime. Parameters for Figs. 3(a) and 3(b) at the front edge of the gas jet yield $G_{SRS} = 40$ and 30, respectively. A larger G_{SRS} for higher intensity interactions is qualitatively consistent with experimental observations. The large $G_{SRS}(\gg 1)$ shows that SRS is fully nonlinear and is observed as modulation of the intensity along z which might be due to bursting behavior of the SRS [17].

A number of two dimensional particle-in-cell simulations were performed using the code OSIRIS [20] in order to understand this interaction. The spatial resolution was 30 cells per laser wavelength in the propagation direction and 16 cells per wavelength in the direction transverse to propagation, with 4 particles per cell for both electrons and mobile ions. The simulation was performed in a stationary box of size 400 μm by 200 μm. A Gaussian laser pulse propagates along the z axis with a peak a_0 of 1.5 and a pulse length of $\tau = 42$ fs. The radius of the laser pulse was 12.7 μm FWHM at the front edge of the plasma. The plasma density profile was assumed to be flat top at a density of $n_e = 1.73 \times 10^{19}$ cm^{-3}. A linear density up ramp with a length of 50 μm was at the front of the plasma. Sequential images from the simulation are shown in Fig. 4 which displays 3 stages of the laser pulse evolution during propagation. In the first stage, Fig. 4(a), the laser pulse is longer than the plasma period ($c\tau > \lambda_p$), and plasma waves due to SRSS are clearly visible at the angle corresponding to the scattered light emitted at an angle given by Eq. (1). In the second stage, Fig. 4(b), the pulse duration has become smaller than the relativistically corrected plasma wavelength, and hence SRSS has ceased. The peak laser a_0 is amplified due to self-focusing and a bubble-shaped wakefield begins to form. In the third stage, Fig. 4(c), a stable, bare ion cavity was formed. A single bubble was observed for this simulation run since the laser spot radius was close to the matched spot size, w_0 ($1/e^2$ intensity radius), given by $k_p w_0 = 2\sqrt{a_0}$ [3]. However, a transversely modulated wakefield could also be observed in simulations for larger spot sizes, at the same peak laser power. Such density modulations could perturb the transverse laser beam profile resulting in laser beam filamentation as well as electron beam filamentation.

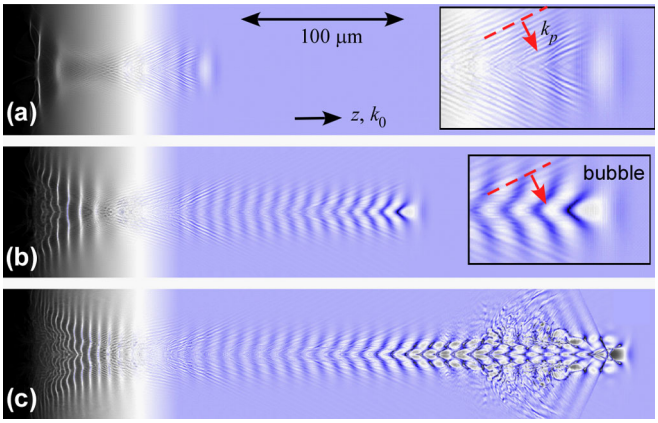

FIG. 4 (color online). Electron density profiles from OSIRIS simulation of a 42 fs pulse with $a_0 = 1.5$. (a) $t = 330$ fs, (b) $t = 660$ fs, (c) $t = 1000$ fs. The dashed line and the arrow show wave front and k_p of the plasma wave. Insets are magnified by twice. Two dashed lines in (a) and (b) have the same $\theta = 63°$, which is consistent with the value obtained from Eq. (1).

We found that the angle $\theta = 63°$ was constant across propagation, which can be seen in the two insets in Fig. 4, which show identical k_p direction. Careful analysis of θ at the density ramp where θ is expected to increase was also 63°. A θ differing from 63° is observed at the density ramp for Figs. 4(b) and 4(c). However, this k_p could not contribute to the SRSS observed in the experiment since no energy from the laser pulse is left ($c\tau \sim 13.5\ \mu$m).

In the linear theory for Raman scattering [19], the growth rate of backward SRS is much greater than that for forward SRS. Therefore, at the beginning of the interaction, backward SRS dominates over the forward such that Eq. (1) is likely not applicable. As the instability evolves, forward SRS grows sufficiently such that Eq. (1) describes the angle of the main emission of SRSS. Higher order plasma waves [21], which are observed in our two-dimensional particle-in-cell simulations, might also play a role for determining a scattering angle where high intensity of the laser pulse is required and which most likely occurs at the beginning of the interaction.

In the simulation, we observed that the laser pulse is not only etched from the front part of the pulse but also from the rear. This is in contrast to other pulse evolution processes in this regime for LWFAs, in which the laser pulse is etched from the front of the pulse due to photon deceleration or pulse front erosion [3]. Since there is a correlation between pulse evolution and SRSS as described above, it is likely that SRSS contributes to the etching of the rear of the pulse. Note that for SRSS, the driven plasma wavelength is much smaller than the wake wavelength $\lambda_p \sim 2\pi\omega_p/c$, such that the many periods fit in the laser pulse because of the phase matching condition which leads to a relatively slow plasma wave phase velocity.

In conclusion, we observed that excessive amounts of SSRS adversely affected the electron beam quality and was correlated with filamentation of the resulting electron beam. The optical side scattered spectrum indicated a clear Stokes shift due to SRSS that is proportional to the relativistically corrected plasma frequency. This can provide a spatially resolved measure of the intensity of the laser beam as it propagates through the plasma. The two-dimensional particle-in-cell simulations in a stationary box show that the laser pulse evolves significantly during propagation through the plasma and SRSS erodes the rear part of the pulse, contributing to the reshaping of the laser pulse to the matched pulse duration. Experiments and simulations both show that using an improved focal spot quality whose size is close to the matched spot size can reduce filamentation due to SRSS and improve electron beam quality. In fact, in these situations SRSS can play a beneficial role in the further evolution of the laser pulse shape towards the matched condition. However it is also clear that longer (unmatched) laser pulses with focal regions having large transverse dimensions can result in significant SRSS that can generate perturbations in the beam, thus seeding filamentation instabilities.

This work was supported by the U.S. National Science Foundation through the Physics Frontier Center FOCUS (Grant No PHY-0114336) and NSF/DNDO Grants No. 0833499 and No. 0903557. The authors would like to acknowledge the OSIRIS Consortium, consisting of UCLA and IST (Lisbon, Portugal), for the use of OSIRIS.

*Present address: Dynamical Experiments Group, Propulsion Division, Soreq NRC, Yavnee 81800, Israel.

[1] T. Tajima and J. M. Dawson, Phys. Rev. Lett. **43**, 267 (1979).
[2] A. Pukhov *et al.*, Plasma Phys. Controlled Fusion **46**, B179 (2004).
[3] W. Lu *et al.*, Phys. Rev. ST Accel. Beams **10**, 061 301 (2007).
[4] S. P. D. Mangles *et al.*, Nature (London) **431**, 535 (2004).
[5] J. Faure *et al.*, Nature (London) **431**, 541 (2004).
[6] C. G. R. Geddes *et al.*, Nature (London) **431**, 538 (2004).
[7] W. P. M. Leemans *et al.*, Nature Phys. **2**, 696 (2006).
[8] J. Faure *et al.*, Nature (London) **444**, 737 (2006).
[9] S. Kneip *et al.*, Phys. Rev. Lett. **103**, 035002 (2009).
[10] A. B. Borisov *et al.*, Phys. Rev. Lett. **68**, 2309 (1992).
[11] G. S. Sarkisov *et al.*, Phys. Rev. E **59**, 7042 (1999).
[12] A. G. R. Thomas *et al.*, Phys. Rev. Lett. **98**, 095004 (2007).
[13] J. E. Ralph *et al.*, Phys. Rev. Lett. **102**, 175003 (2009).
[14] A. G. R. Thomas *et al.*, Plasma Phys. Controlled Fusion **51**, 024 010 (2009).
[15] A. G. R. Thomas *et al.*, Phys. Rev. Lett. **98**, 054802 (2007).
[16] S. W. Bahk *et al.*, Opt. Lett. **29**, 2837 (2004).
[17] G. Shvets *et al.*, Phys. Plasmas **4**, 1872 (1997).
[18] D. W. Forslund *et al.*, Phys. Rev. Lett. **54**, 558 (1985).
[19] J. F. Drake *et al.*, Phys. Fluids **17**, 778 (1974).
[20] R. A. Fonseca *et al.*, Lect. Notes Comput. Sci. **2331**, 342 (2002).
[21] H. C. Barr *et al.*, Phys. Rev. Lett. **81**, 2910 (1998).